**Naval Research Laboratory**
Washington, DC 20375-5320

NRL/MR/6410--01-8554

# Design of Nozzle for UV Fluorescence Detector

RAVI RAMAMURTI

*Center for Reactive Flow and Dynamical Systems Branch*
*Laboratory for Computational Physics and Fluid Dynamics*

May 17, 2001

# REPORT DOCUMENTATION PAGE

*Form Approved*
*OMB No. 0704-0188*



| 1. AGENCY USE ONLY (*Leave Blank*) | 2. REPORT DATE | 3. REPORT TYPE AND DATES COVERED |
|---|---|---|
| | May 17, 2001 | Memorandum Report |

4. TITLE AND SUBTITLE

Design of Nozzle for UV Fluorescence Detector

5. FUNDING NUMBERS

6. AUTHOR(S)

Ravi Ramamurti

7. PERFORMING ORGANIZATION NAME(S) AND ADDRESS(ES)

Naval Research Laboratory
Washington, DC 20375-5320

8. PERFORMING ORGANIZATION REPORT NUMBER

NRL/MR/6410--01-8554

9. SPONSORING/MONITORING AGENCY NAME(S) AND ADDRESS(ES)

10. SPONSORING/MONITORING AGENCY REPORT NUMBER

11. SUPPLEMENTARY NOTES

12a. DISTRIBUTION/AVAILABILITY STATEMENT

Approved for public release; distribution is unlimited.

12b. DISTRIBUTION CODE

13. ABSTRACT (*Maximum 200 words*)

The flow through the nozzle of a Ultra-Violet (UV) Fluorescence detector is computed. The primary goal of this project is to study the flow exiting the nozzle and predict the spreading of the flow at a specified distance from the exit of the nozzle. The unstructured mesh-based incompressible flow solver, *FEFLO*, is used to compute this flow. Computed pressure drops across the nozzle are compared with experiment and shows good agreement. Several computations are performed varying the flow rates through the nozzle and the position of the inner capillary tube with respect to the exit of the nozzle. The effect of these parametric variations on the spreading rate of the flow is studied. This will serve to design the nozzle configuration and optimum flow condition.

14. SUBJECT TERMS

Nozzle UV fluorescence Unstructured grid

15. NUMBER OF PAGES

26

16. PRICE CODE

| 17. SECURITY CLASSIFICATION OF REPORT | 18. SECURITY CLASSIFICATION OF THIS PAGE | 19. SECURITY CLASSIFICATION OF ABSTRACT | 20. LIMITATION OF ABSTRACT |
|---|---|---|---|
| UNCLASSIFIED | UNCLASSIFIED | UNCLASSIFIED | UL |

NSN 7540-01-280-5500

Standard Form 298 (Rev. 2-89)
Prescribed by ANSI Std 239-18
298-102

CONTENTS

# Design of Nozzle for UV Fluorescence Detector

## INTRODUCTION

Monitoring biological aerosols is important and has application to DoD, medical and health, food processing and environmental monitoring communities. An optical Ultra Violet (UV) fluorescence detector has been developed by the Optical Sciences Division of NRL (Code 5615) for this purpose. The detector consists of an inlet nozzle which directs sample particles to the focus of an elliptical mirror. A red laser beam illuminates the flow at this focal plane and the scatter red light triggers a pulsed UV laser. The UV fluorescence from the aerosol is then detected and then correlated to the aerosol concentration.

The nozzle employed in the UV fluorescence detector is similar to a pitot tube in construction. An inner capillary tube carries the particulate flow while the outer tube carries a sheath flow. The outer tube ends in a tapered nozzle and the inner tube may either be flush with the exit or recessed inside the nozzle. In the present study, we perform computation of flow exiting the nozzle to determine the spreading of the flow at a specified distance from the exit of the nozzle where the red laser beam is directed. A series of computations are performed varying the distance by which the inner tube is recessed and the flow rates through the nozzle and study the effect on the spreading rate of the exiting flow.

## INCOMPRESSIBLE FLOW SOLVER

*FEFLO* is a finite element-based incompressible flow solver based on simple, low-order elements. The simple elements enable the flow solver to be as fast as possible reducing the overhead in building element matrices, residual vectors etc. The governing equations are written in Arbitrary Lagrangian Eulerian form which enables simulation of flow with moving bodies. For high Reynolds number flow cases, the mesh requirement is met by employing arbitrary semi-structured grids close to wetted surfaces and wakes. The full details of the flow solver, the rigid body motion and adaptive remeshing are given by Ramamurti et al.[1] and are summarized next.

The governing equations employed are the incompressible Navier-Stokes equations in Arbitrary Lagrangian Eulerian (ALE) formulation. They are written as

$$\frac{D\mathbf{v}}{Dt} + \mathbf{v}_a \cdot \nabla\mathbf{v} + \nabla p = \nabla \cdot \sigma \tag{1a}$$

$$\frac{D\mathbf{v}}{Dt} = \frac{\partial \mathbf{v}}{\partial t} + \mathbf{w}.\nabla\mathbf{v} \tag{1b}$$

$$\nabla \cdot \mathbf{v} = 0 \tag{2}$$

Here $p$ denotes the pressure, $\mathbf{v}_a = \mathbf{v} - \mathbf{w}$, the advective velocity vector (flow velocity $\mathbf{v}$ minus mesh velocity w), and the material derivative is with respect to the mesh velocity w. Both the pressure $p$ and the stress tensor $\sigma$ have been normalized by the (constant) density $\rho$, and are discretized in time using an implicit time stepping procedure. It is important for the flow solver to be able to capture the unsteadiness of a flow field. The present flow solver is built as time-accurate from the onset, allowing local timestepping as an option. The resulting expressions are subsequently discretized in space using a Galerkin procedure with linear tetrahedral elements. In order to be as fast as possible, the overhead in building element matrices, residual vectors, etc. should be kept to a minimum. This requirement is met by employing simple, low-order elements

Manuscript approved April 9, 2001

that have all the variables (u,v,w,p) at the same location. The resulting matrix systems are solved iteratively using a preconditioned gradient algorithm (PCG). The flow solver has been successfully evaluated for both 2-D and 3-D, laminar and turbulent flow problems by Ramamurti *et al.*[2,3]

## COMPUTATIONAL RESULTS

The nozzle employed in the UV fluorescence detector is similar to a pitot tube in construction and is shown in Fig. 1. An inner capillary tube carries the particulate flow while the outer tube carries a sheath flow. The outer tube ends in a tapered nozzle and the inner tube is flush with the exit of the nozzle. Figure 2 shows the variation of the pressure drop across a nozzle of similar construction for various flow rates. These results were obtained experimentally by J. Eversole of Code 5615. Figures 3a-d show the results of the computations for a total flow rate, $Q_{total}$, of 12Lpm with the inner particulate flow, $Q_{inner}$, of 3Lpm and the outer sheath flow, $Q_{outer}$, of 9Lpm. The computational grid consists of 537K points and 2.9M tetrahedral elements. The surface triangulation, Fig. 3a, shows the grid clustering near the exit of the nozzle. From Fig. 3b, the pressure drop can be seen to be linear inside the nozzle. The computational unit of pressure for the incompressible flow is $m^2/s^2$ ($=p/\rho$), where $\rho$ is the density of air ($Kg/m^3$). The computed pressure drop for this flow is 47.5torr and the experimental value from Fig. 2 is approximately 45.0torr. Figure 3c and 3d show the variation of velocity near the exit of the nozzle. It can be seen that the inner and outer flows are nearly parallel with minor instabilities present near the edges of the outer flow.

The nozzle geometry was next updated and is shown in Fig. 4. The inner capillary tube in this configuration has a taper and the inner diameter of the outer tube is also reduced to 4.0mm. The experimentally observed pressure drop for this nozzle is shown in Fig. 5. Computations were performed for three different flow rates, 4Lpm, 8Lpm and 12Lpm. The inner and outer flow rates are prescribed for these computations. For a $Q_{total}$ = 4Lpm, the prescribed flow rates were $Q_{inner}$ = 1.5Lpm and $Q_{outer}$ = 2.5Lpm; for $Q_{total}$ = 8Lpm, the prescribed flow rates were $Q_{inner}$ = 2.5Lpm and $Q_{outer}$ = 5.5Lpm; for $Q_{total}$ = 12Lpm, $Q_{inner}$ = 3.0Lpm and $Q_{outer}$ = 9.0Lpm. The computed pressure drops for the inner and outer flows are shown in Fig. 6. The average pressure drop across the entire nozzle is computed as an area weighted average of the pressure drops of the inner and outer flows. The pressure drop for the inner flow increases from 12.3torr to 47.4torr as the inner flow rate $Q_{inner}$ is increased from 1.5Lpm to 3.0Lpm. For the outer flow, the $\Delta p$ drops from 38.65torr to 0.7torr as $Q_{outer}$ is increased from 2.5Lpm to 5.5Lpm. At $Q_{total}$ = 12Lpm, the computational pressure drop is 47.4torr compared to 45.0 in the experiments. The prescribed computational flow rates are $Q_{inner}$ = 3Lpm and $Q_{outer}$ = 9Lpm, whereas the experimentally observed flow rates are 2.5Lpm and 8.0Lpm, approximately. It should be noted that these flow rates do not add up to the total flow rate of 12.0Lpm. For a total flow rate of 8Lpm, the computational pressure drop is 38.8torr compared to 23.0torr observed in the experiments. The prescribed $Q_{inner}$ and $Q_{outer}$ for this case are 2.5Lpm and 5.5Lpm, respectively. Again, there is a discrepancy in the experimentally observed inner and outer flow rates and the total flow rate by approximately 0.75Lpm. At $Q_{total}$ = 4Lpm, the computational pressure drop is 12.3torr compared to 8.0torr observed in the experiments. These differences may be due the experimental errors in measuring the flow rates and the experimental error is not known. The prescribed $Q_{inner}$ and $Q_{outer}$ for this case are 1.5Lpm and 2.5Lpm, respectively.

Next, the position of the exit of the inner capillary tube is recessed by 5.0mm and 10.0mm the computations are performed for these configurations for the three flow rates. Figures 7a-c show the variation of the centerline pressure for the three different nozzle configurations. It can be seen that as the flow rate is increased, the pressure drop across the nozzle increases, as would be expected. The effect of the capillary recession on the centerline pressure distribution is shown in

Figs. 8a-c. For a flow rate of 4Lpm, Fig. 8a, the pressure drop for the case where the capillary is recessed by 5mm exceeds that of the flush and the 10mm cases. This trend is reversed as the flow rate is increased to 8Lpm and 12Lpm. For all the three flow rates studied, the pressure drop for the 10mm case is higher than the flush capillary. In order to understand the reason for the trend reversal for the 5mm case, the details of the flow for these cases are examined. Figures 9 and 10 show the variation of pressure drop with flow rate when the inner capillary tube is recessed by 5.0mm and 10.0mm, respectively. From Figure 9, it can be seen that the pressure drop across the inner capillary increases as the flow rate is increased from 1.5Lpm to 2.5Lpm and remains almost same for a flow rate of 5.5Lpm. The pressure drop for the outer flow behaves similar to that of the flush capillary case. Figure 10 shows that the $\Delta p$ increases almost linearly with flow rate.

Figure 11 shows the surface definition and the triangulation of the nozzle geometry with flush capillary. The computational mesh consists of 242K points and 1.2M tetrahedral elements. Figure 12 shows the results of the computation for this configuration at a flow rate of 12Lpm. The pressure drop inside the nozzle is almost linear, Fig. 12a, and is almost constant after the exit of the nozzle. The flow exiting the nozzle is parallel as can be seen from the velocity contours, velocity vectors and particle traces, Figs. 12b-d. Figure 13a shows the particle traces for the nozzle with flush capillary at 4Lpm, and the flow exiting is nearly parallel, and the outer sheath flow exhibits a divergence, which is not of primary interest of the study. Figure 14 shows the geometry of the nozzle with the capillary tube recessed from the exit of the nozzle. Figures 15a and b show the pressure inside the nozzle and the velocity vectors near the exit, for a nozzle with the capillary recessed by 5.0mm. It is clear that at the edge of the inner particulate flow, shear layer instability is present. This is also evident in the particle traces shown in Figs. 16a-c, and is present for all the three flow rates studied. Figure 17 shows the contours of the magnitude of velocity outside the capillary tube and the nozzle exit. The capillary tube is recessed by 10.0mm in this case, and the flow exiting it is nearly parallel. Figures 18a-c show the particle traces for this configuration at three different flow rates. In all the cases, the particulate flow is nearly parallel, and the sheath flow shows a small instability at the outer edge of the shear layer. Figures 19-21 show the particle traces for the three different nozzle configurations and for the minimum and maximum flow rates considered in this study. The particles traces shown are released at 0.2mm, 0.4mm and 0.6mm from the centerline of the nozzle. For this nozzle, the inner radius of the capillary is 0.375mm and that of the nozzle is 2.0mm, Fig. 4. For the nozzle with the flush capillary tube, Figs. 19a and b, it can be seen that the inner flow is convergent in the vicinity of the nozzle exit. Particles released at 0.6mm stray away from the centerline in the vicinity of the exit and are drawn to the core flow downstream. As the flow rate is increased, the tendency for the outer flow to spread is reduced. For the case of the nozzle with the capillary recessed by 5.0mm, Figs. 20a and b, the inner the flow exhibits shear layer instability. In this case also, the particles released at 0.6mm tend to spread more at lower flow rates and are drawn to the inner flow as the flow rate is increased. For the nozzle configuration with the capillary recessed by 10.0mm, Figs. 21a and b, the inner flow remains parallel and the particles released at 0.6mm moved closer to the inner flow as the flow rate is increased. The particle traces in the region illuminated by the red laser beam is shown in Figs. 22a and b. At lower flow rate of $Q_{total}$ = 4Lpm, Fig. 22a, the particle released at 0.4mm shows a small instability for the flush capillary and the 5.0mm recessed case. As the capillary is recessed even more, this instability disappears, but the spreading rate of the inner flow is increased. At a higher flow rate of 12Lpm, Fig. 22b, the instability is not evident. As the flow rate is increased, the inner flow becomes more convergent for the nozzle with the flush. For the nozzle with the capillary recessed by 10.0mm, the spreading rate seems to be independent of the flow rate.

## CONCLUSIONS AND RECOMMENDATIONS

The incompressible flow solver *FEFLO* was used to compute the flow through the nozzle of a UV Fluorescence detector. Computed pressure drop for the nozzle is compared with experiments and is in good agreement. Three different nozzle configurations were studied by varying the distance by which the inner capillary tube is recessed. For each of these configurations, the flow rate through the nozzle was varied. The spreading rate of the flow exiting the nozzle was computed. For the nozzle with the flush capillary tube, the inner flow remains convergent and as the flow rate is increased for this configuration, it also becomes stable. For the nozzle with the capillary recessed by 5.0mm, the inner and outer flows exhibit shear layer instability, for all the flow rates considered, and for this reason may not be desirable. The nozzle with the capillary recessed by 10.0mm shows the least instability of the inner flow, although the spreading rate is higher than the other two cases. The spreading rate is also nearly independent of the flow rate, and may be the most desirable of all the three cases considered in this study.

## ACKNOWLEDGEMENTS

This work was supported by the Office of Naval Research through the NRL project on UV Fluorescence detector. The authors would like to thank Dr. Jay Eversole of Code 5615, NRL for the helpful discussions throughout the course of the project. This work was supported in part by a grant of HPC time from the DoD HPC centers, ARL MSRC SGI-O2K and NRL SGI-O2K.

## REFERENCES

1. Ramamurti, R., Sandberg, W.C. and Löhner, R., "Simulation of a Torpedo Launch Using a 3-D Incompressible Finite Element Flow Solver and Adaptive Remeshing," AIAA Paper No. 95-0086, January 1995.

2. Ramamurti, R. and Löhner, R., "Evaluation of an Incompressible Flow Solver Based on Simple Elements," *Advances in Finite Element Analysis in Fluid Dynamics*, 1992, FED Vol. 137, Editors: M.N Dhaubhadel et al., *ASME* Publication, New York, pp. 33-42.

3. Ramamurti, R., Löhner, R. and Sandberg, W.C., "Evaluation of Scalable 3-D Incompressible Finite Element Solver," *AIAA Paper* No. 94-0756, 1994.

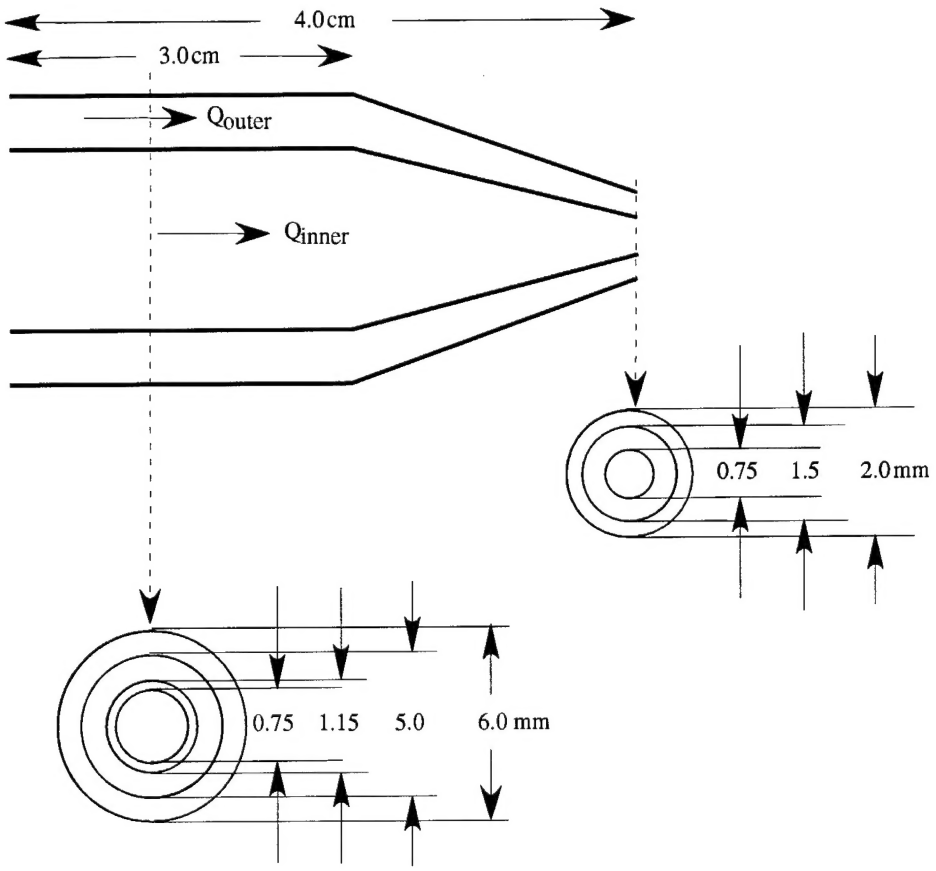


Figure 1. Nozzle geometry

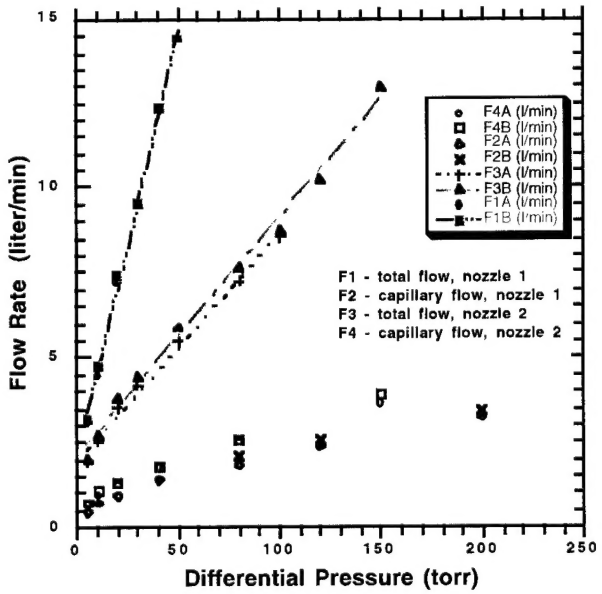


Figure 2. Experimental pressure drop for a similar nozzle

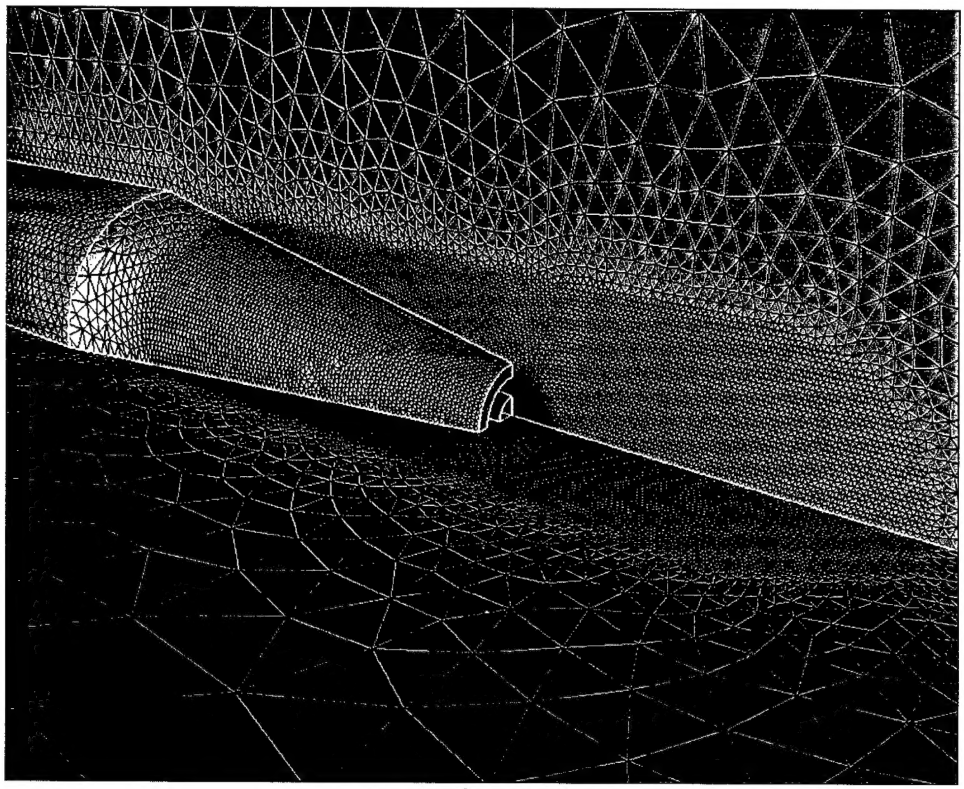

a. Surface mesh

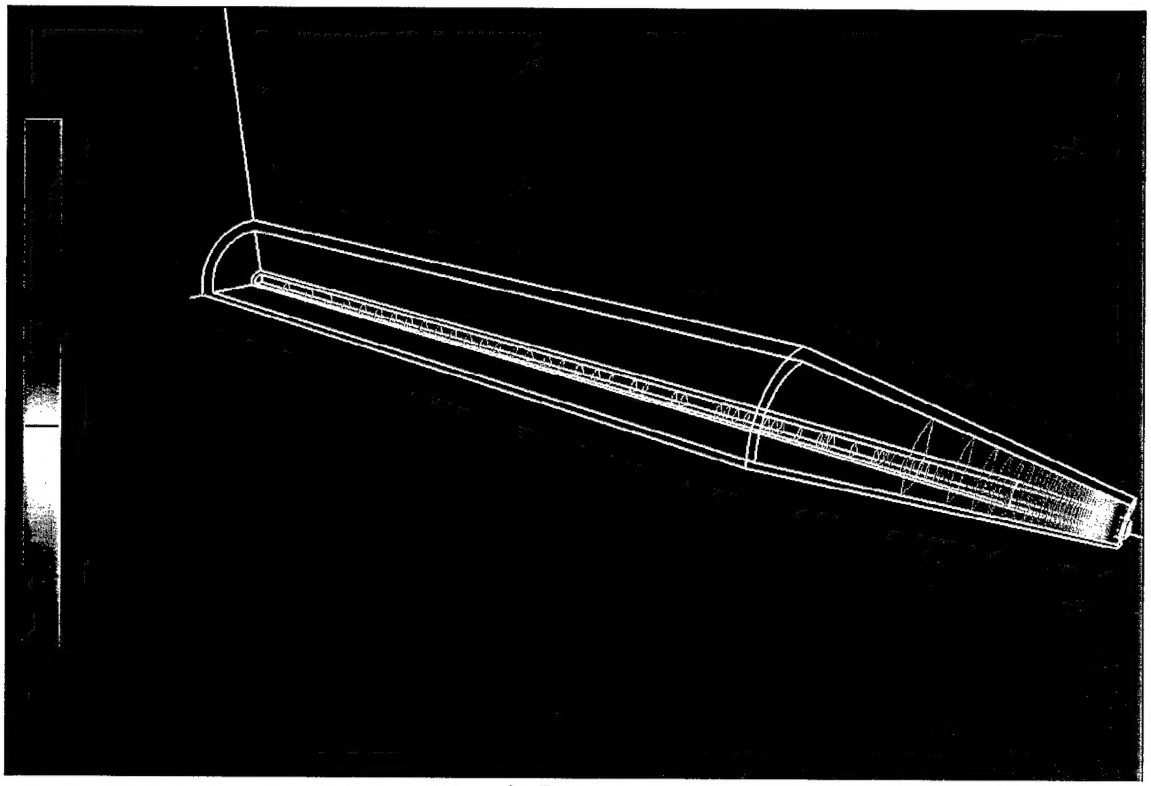

b. Pressure

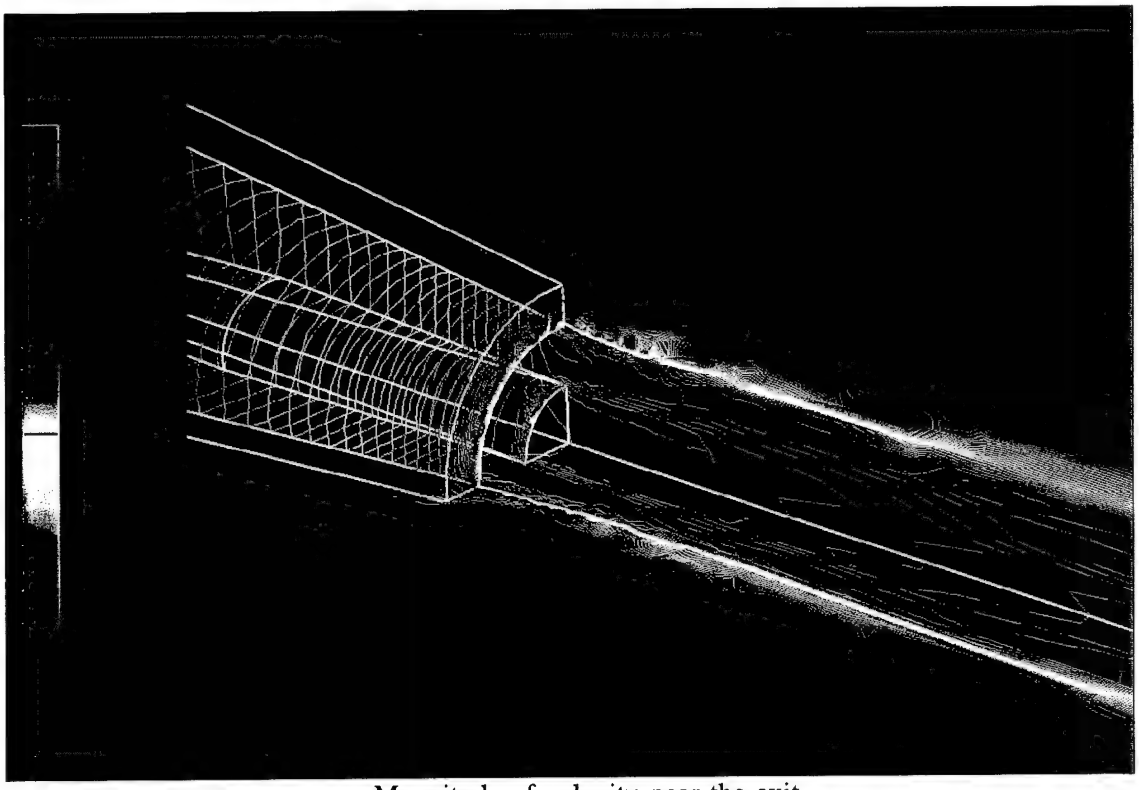

c. Magnitude of velocity near the exit

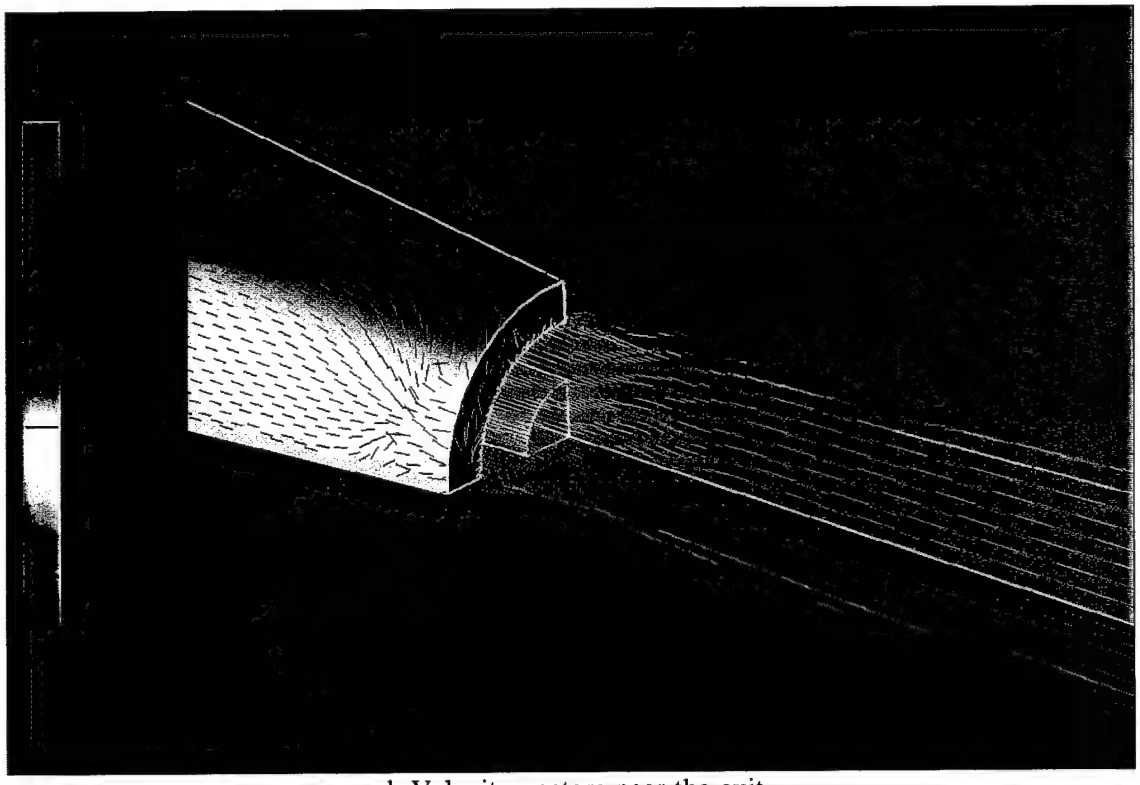

d. Velocity vectors near the exit

Figure 3. Flow through the nozzle, $Q_{total}$ = 12Lpm

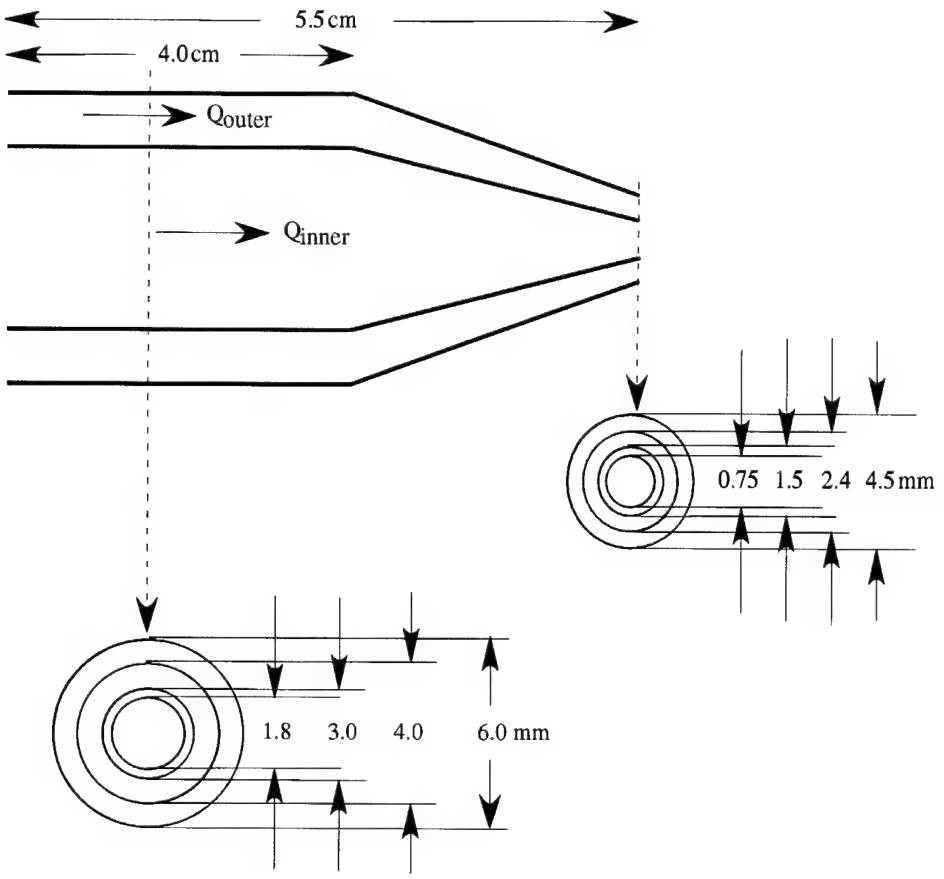


Figure 4. Updated Nozzle Geometry

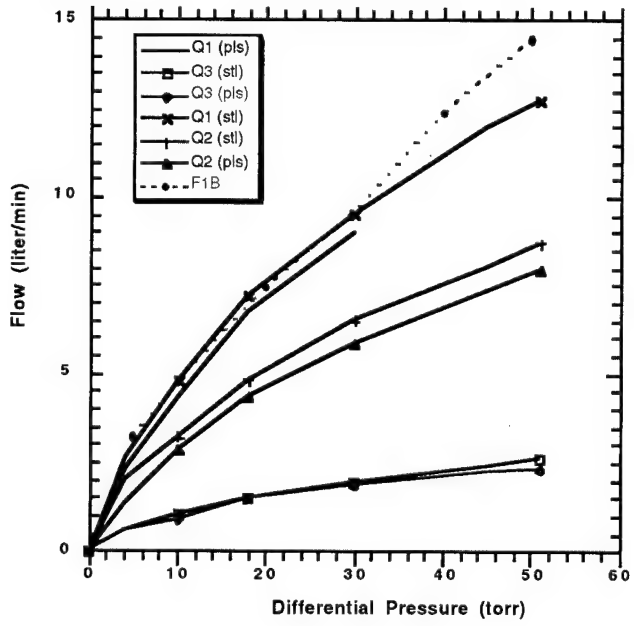


Figure 5. Experimental pressure drop across the nozzle

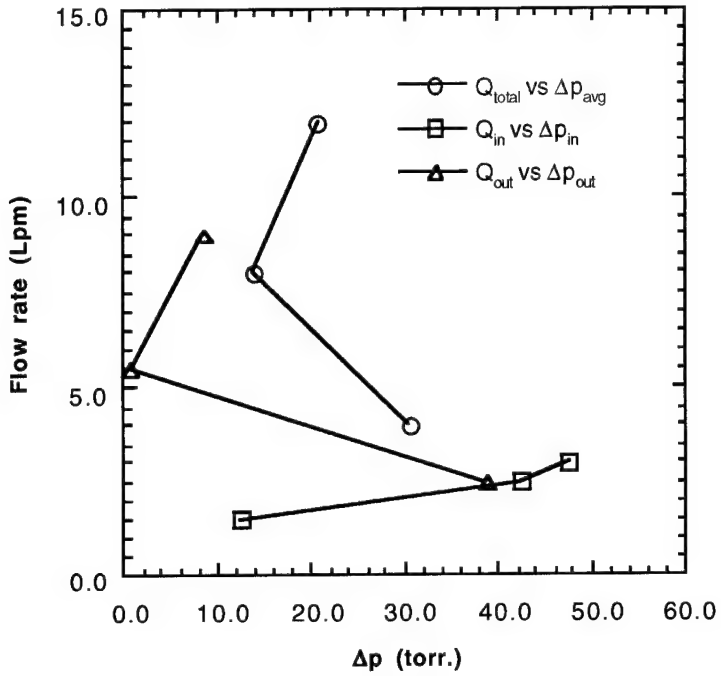


Figure 6. Computed pressure drop

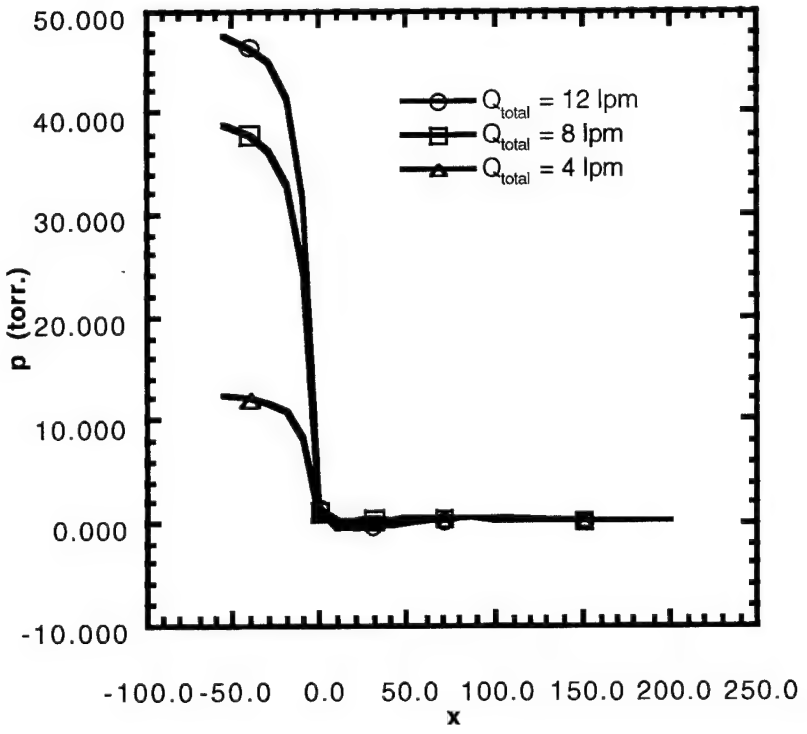


a. Flush capillary

Figure 7. Effect of flow rate on centerline pressure

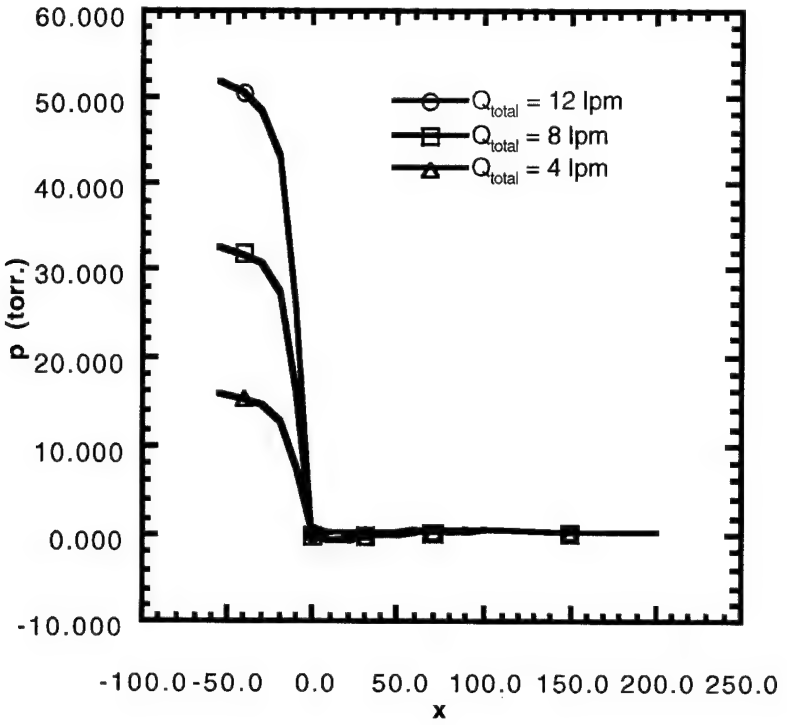


b. Capillary at 5.0mm

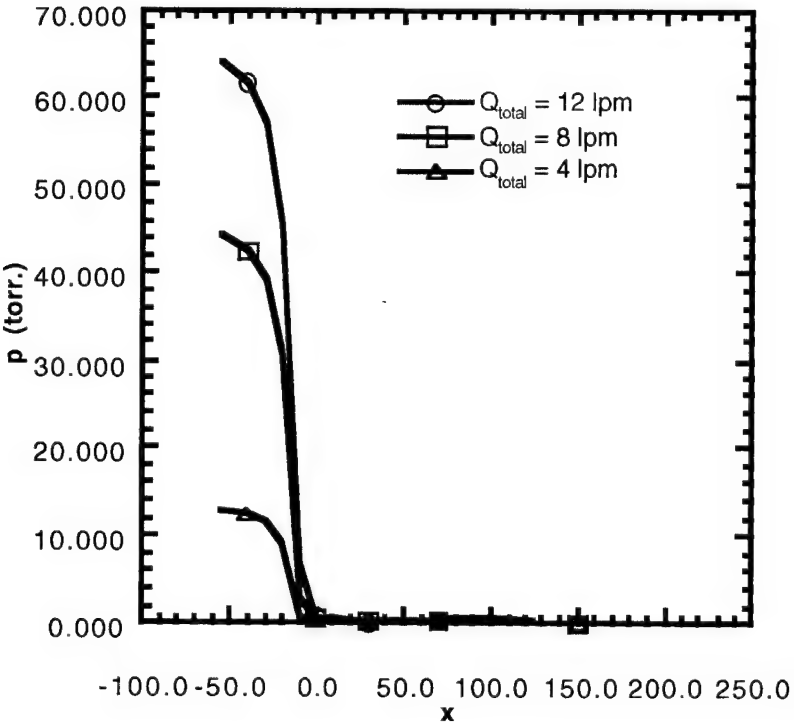


c. Capillary at 10.0mm

Figure 7. Effect of flow rate on centerline pressure

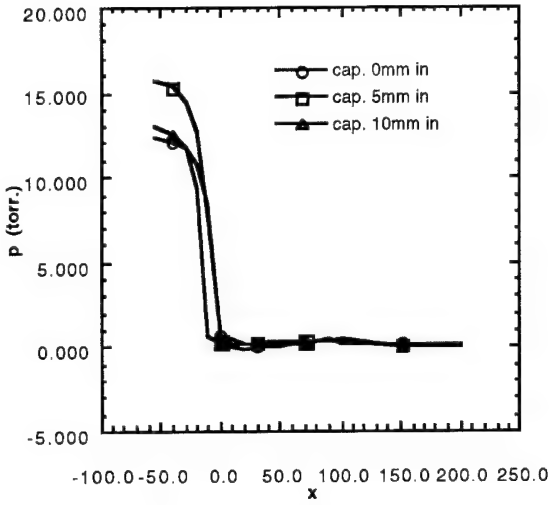


a. $Q_{total}$ = 4Lpm

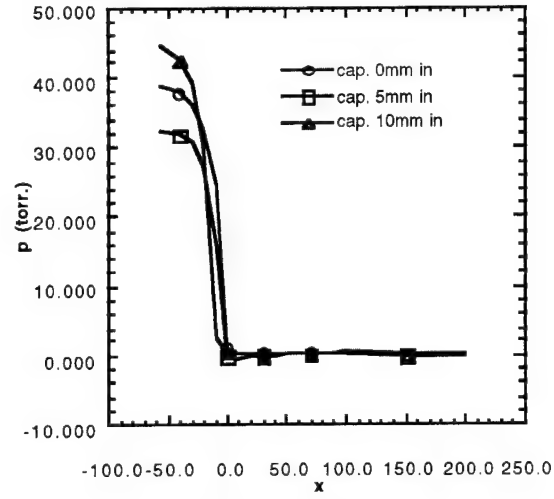


b. $Q_{total}$ = 8Lpm

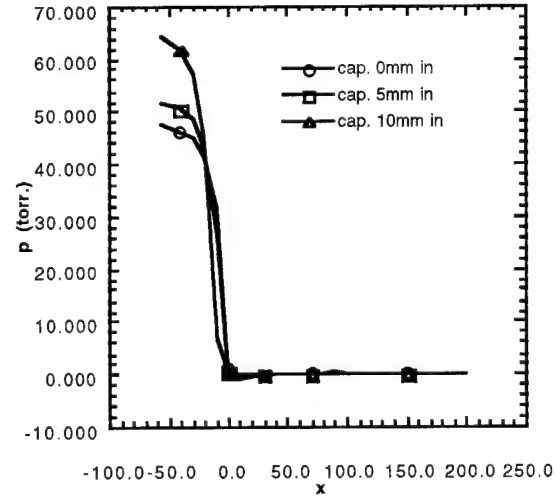


c. $Q_{total}$ = 12Lpm

Figure 8. Effect of capillary position on centerline pressure

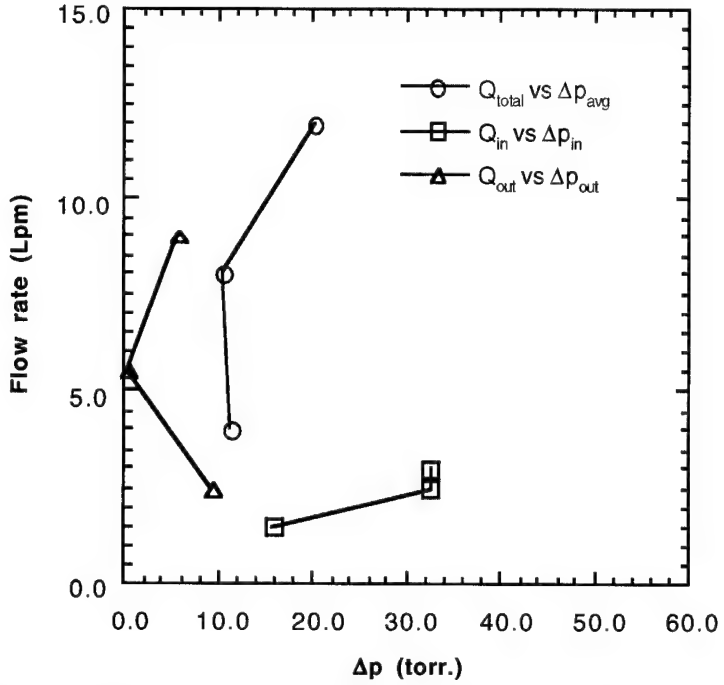


Figure 9. Effect of flow rate on the pressure drop, capillary at 5.0mm

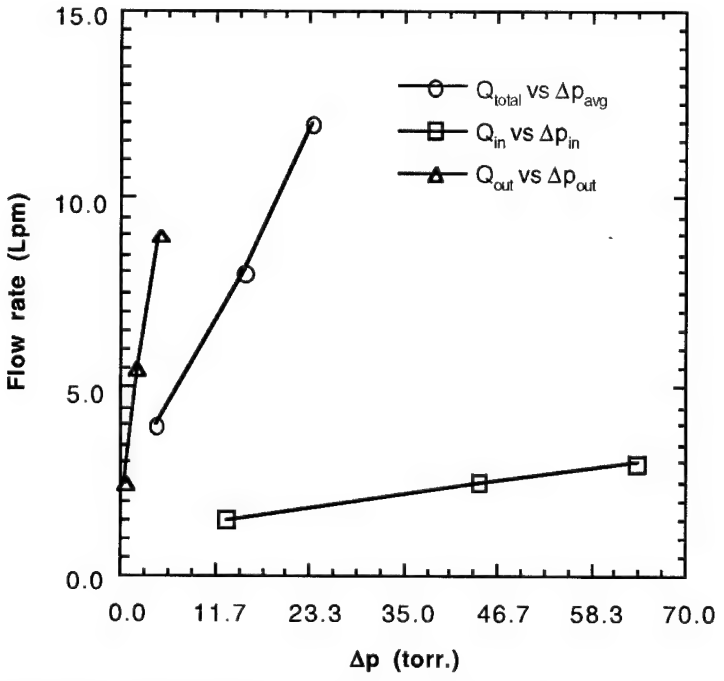


Figure 10. Effect of flow rate on the pressure drop, capillary at 10.0mm

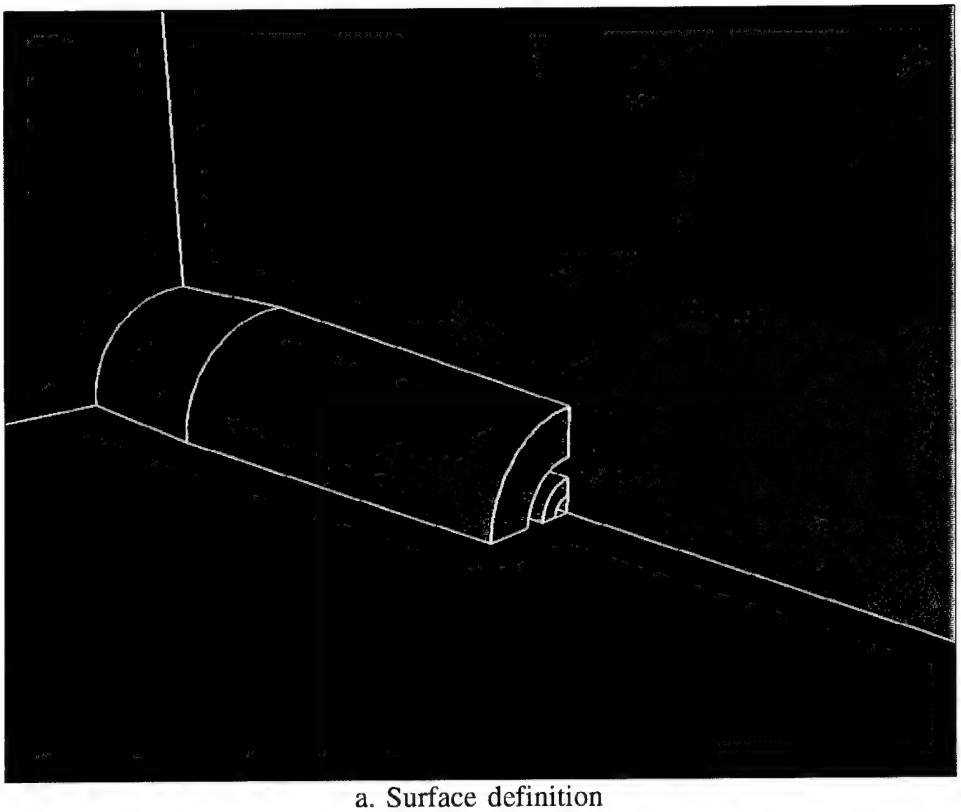

a. Surface definition

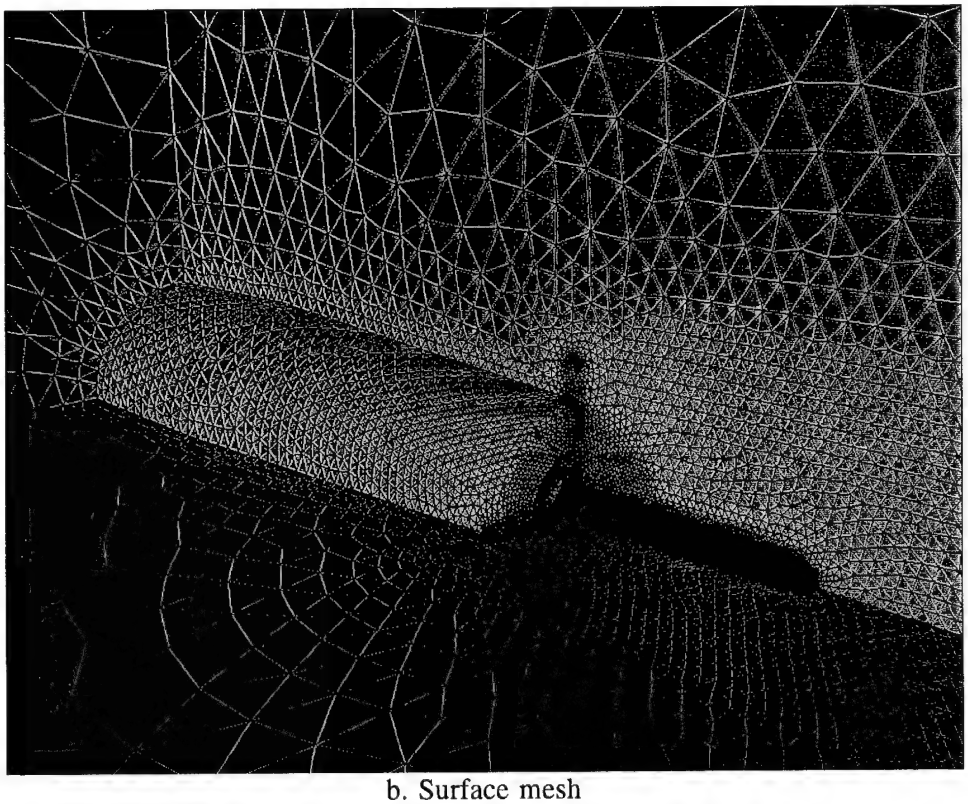

b. Surface mesh

Figure 11. Nozzle geometry

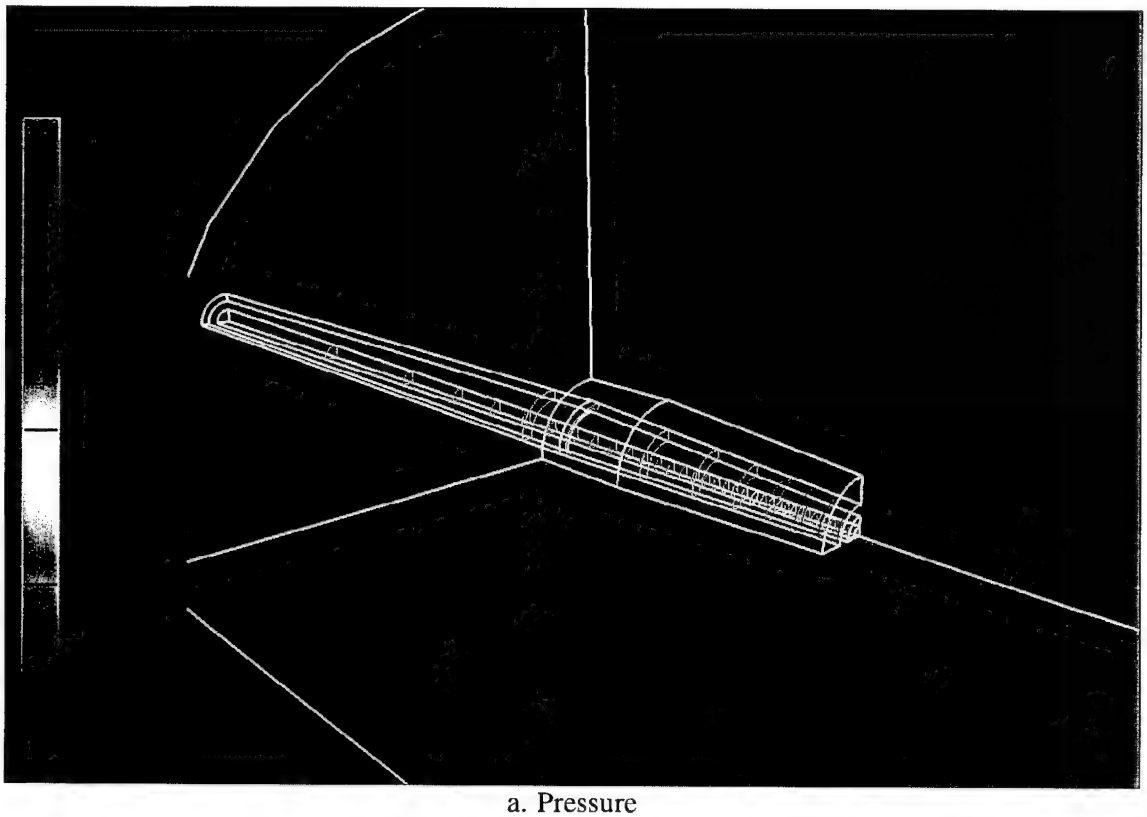

a. Pressure

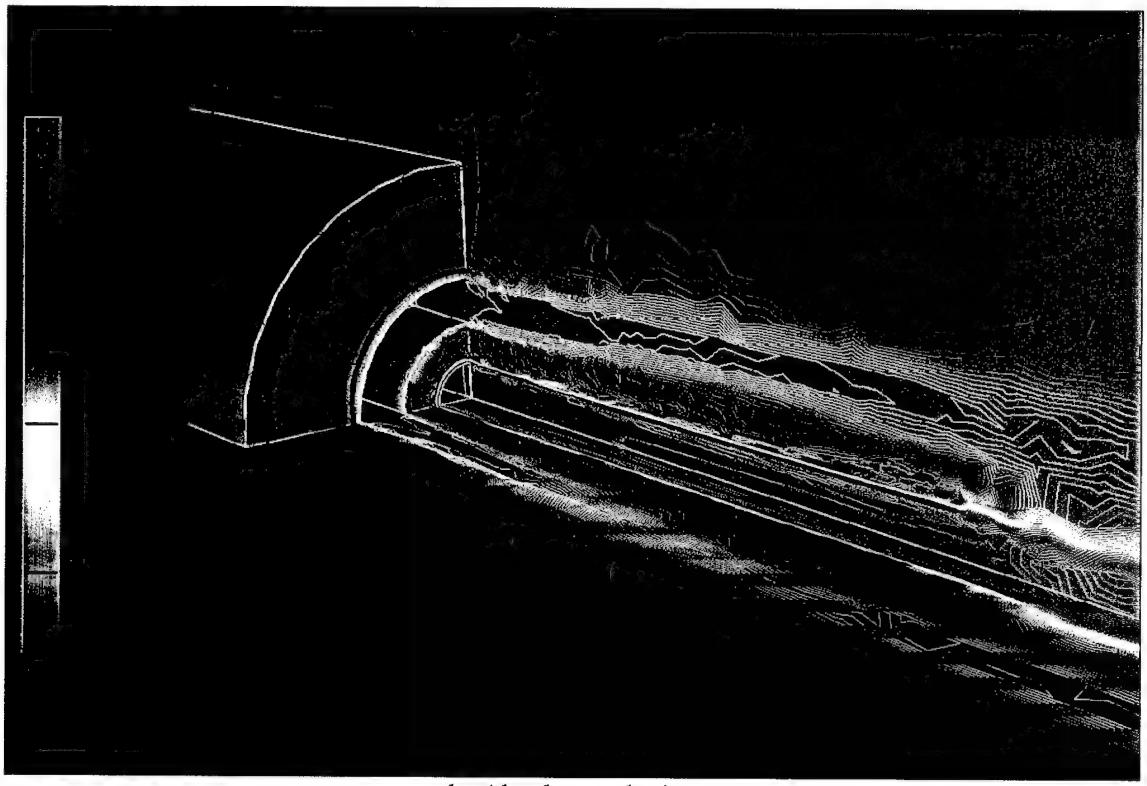

b. Absolute velocity

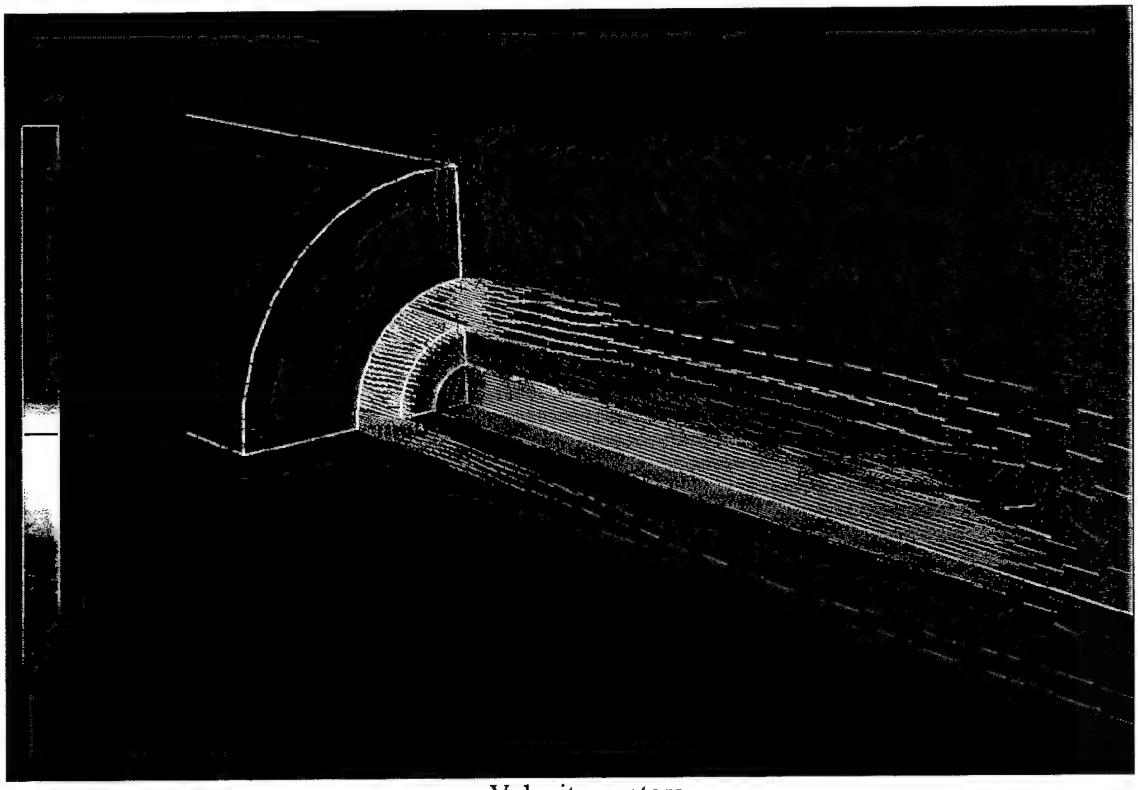

c. Velocity vectors

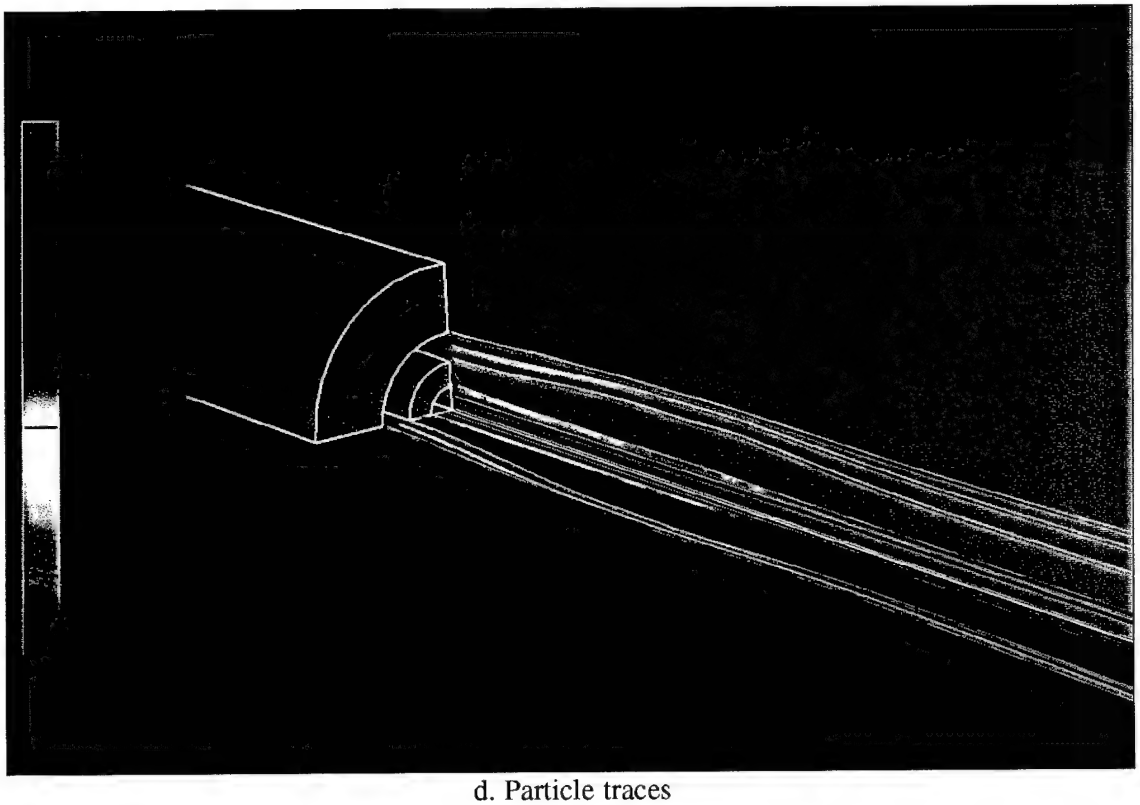

d. Particle traces

Figure 12. Flow through the nozzle with flush capillary, $Q_{total}$ = 12Lpm

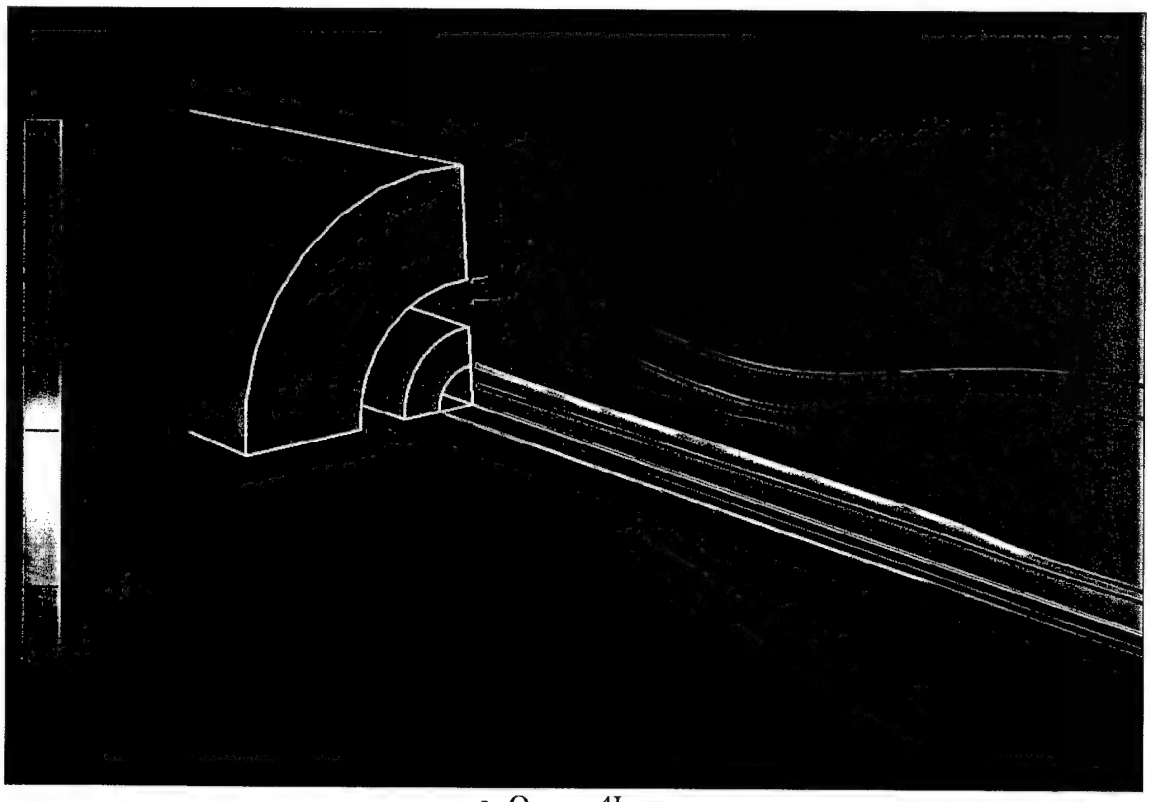

a. $Q_{total}$ = 4Lpm

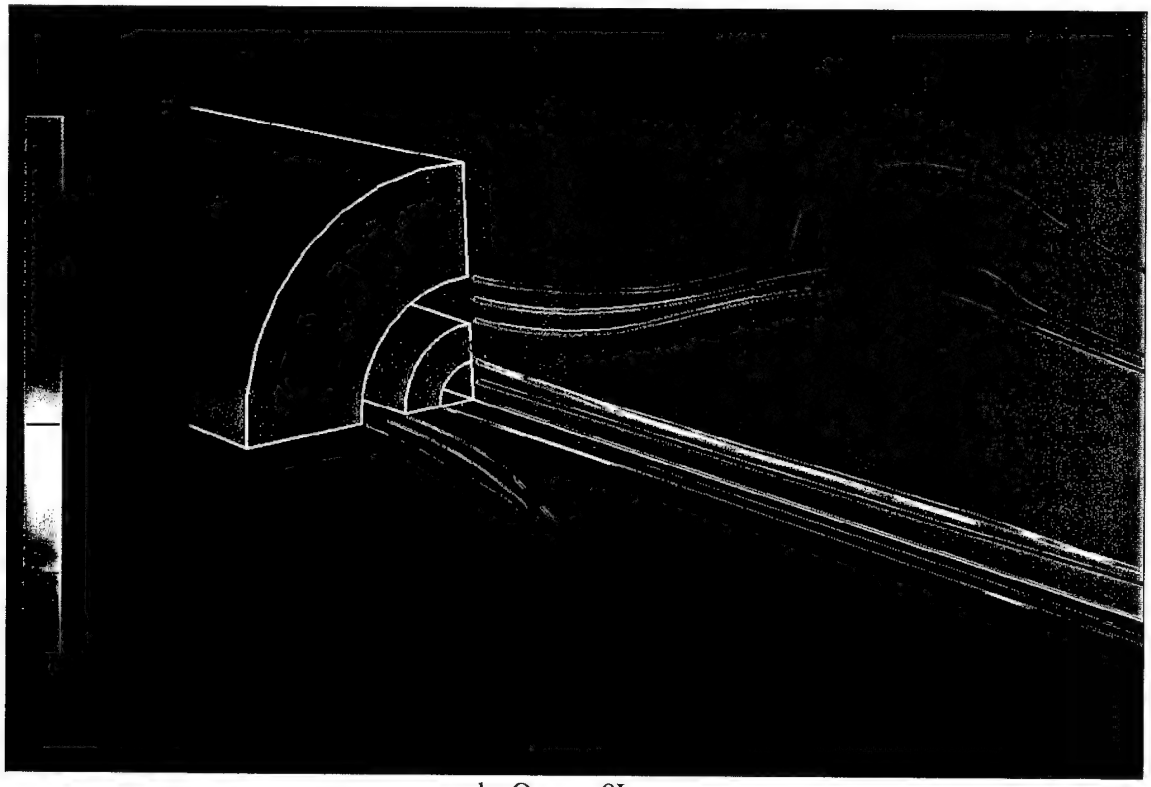

b. $Q_{total}$ = 8Lpm

Figure 13. Particle traces for nozzle with flush capillary

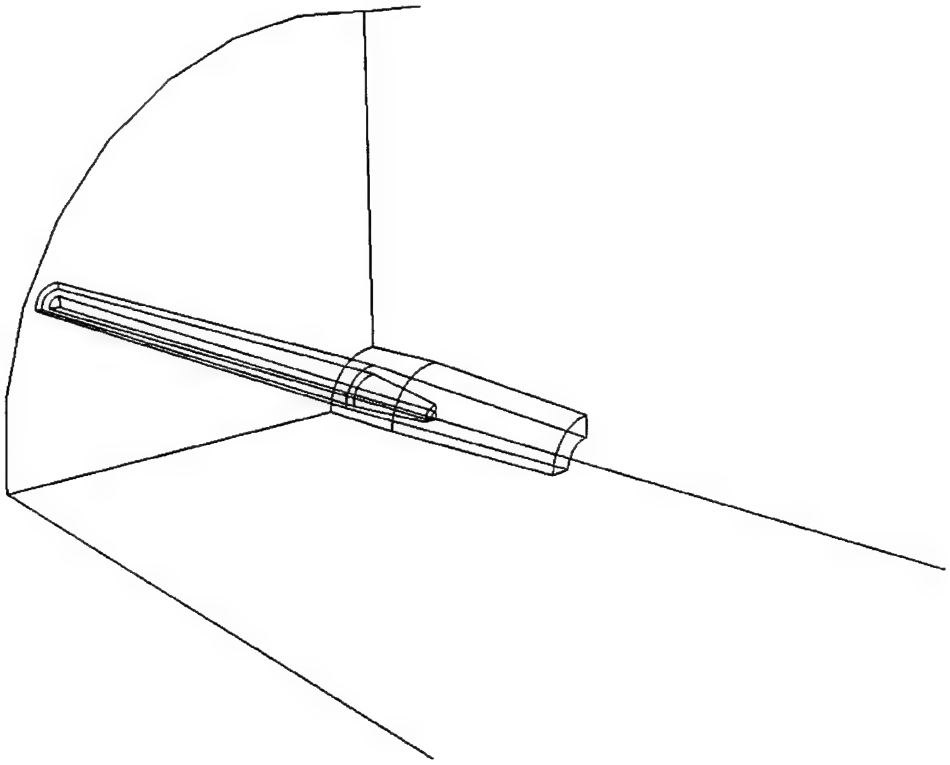

Figure 14. Geometry of the nozzle with capillary moved inside the exit

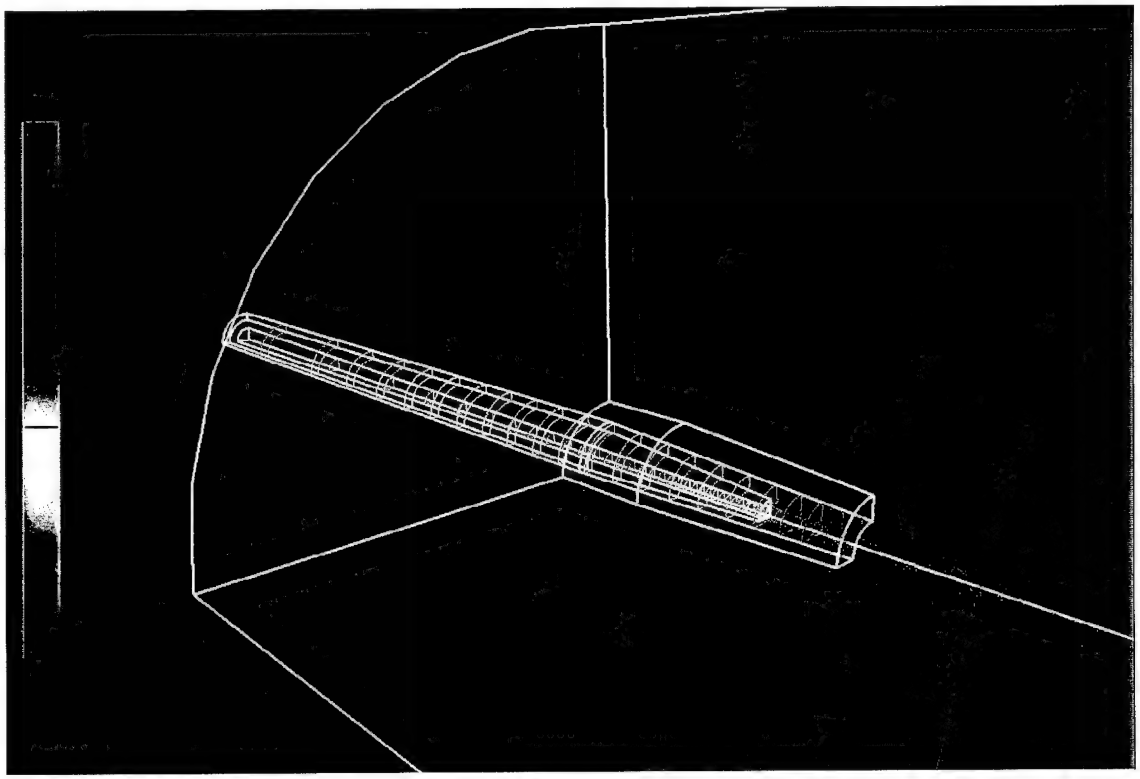

a. Pressure

Figure 15. Flow through the nozzle with capillary moved in 5.0mm, $Q_{total}$ = 4Lpm

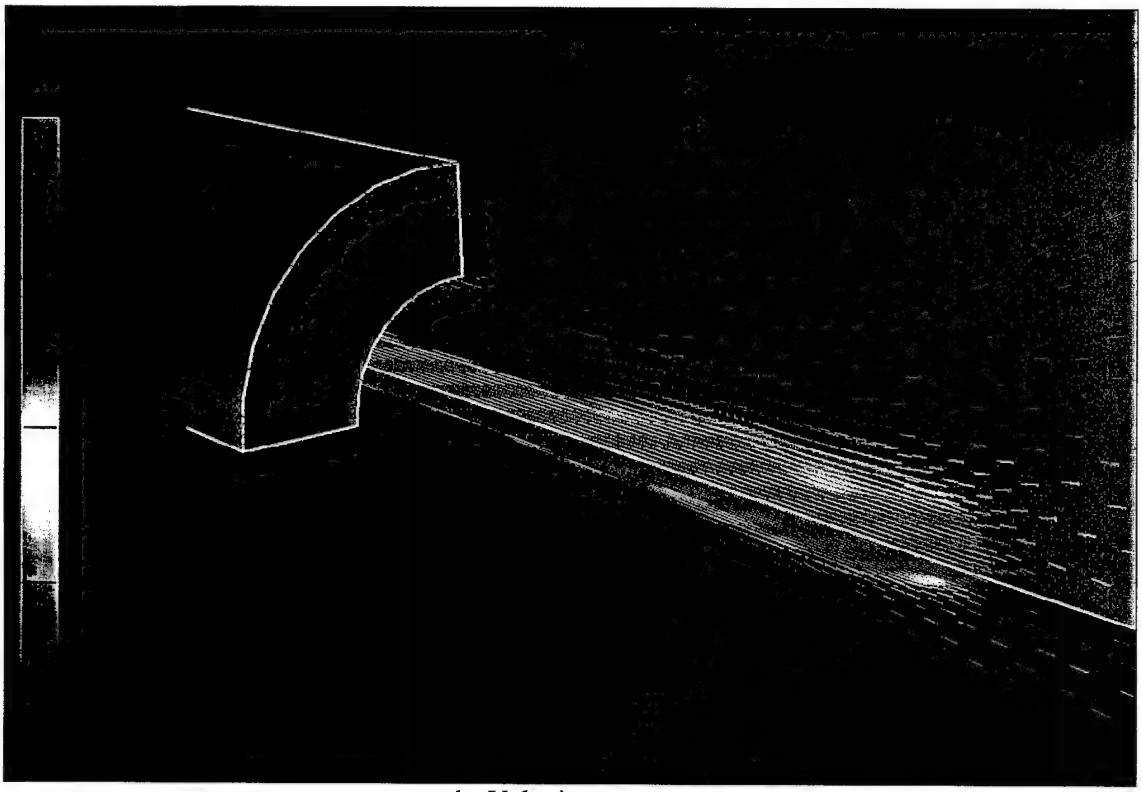

b. Velocity vectors

Figure 15. Flow through the nozzle with capillary moved in 5.0mm, $Q_{total}$ = 4Lpm

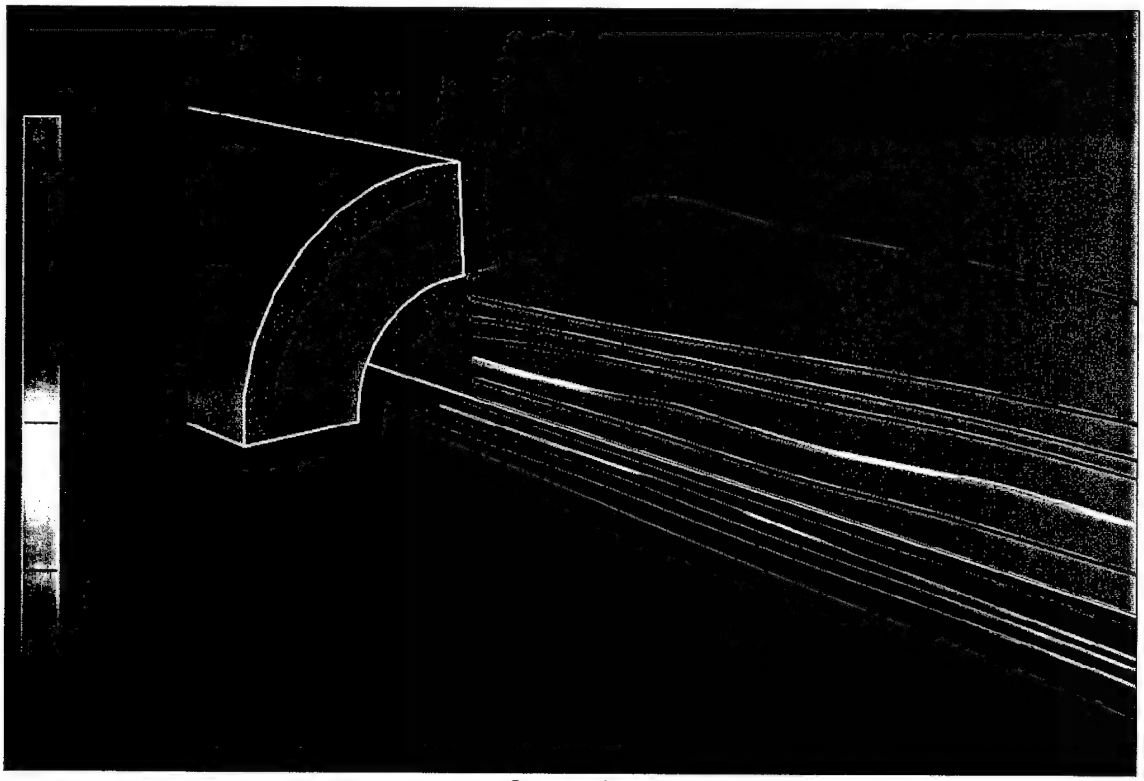

a. $Q_{total}$ = 4Lpm

Figure 16. Particle traces for nozzle with capillary moved in 5.0mm

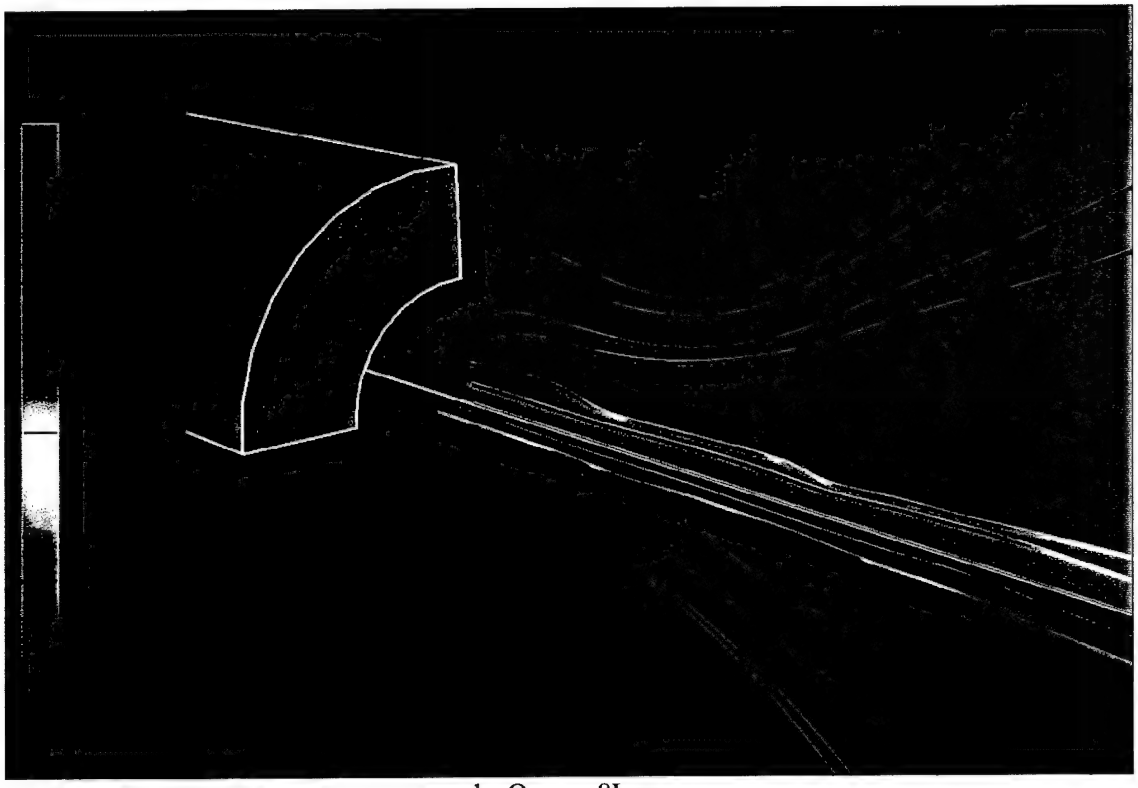

b. $Q_{total}$ = 8Lpm

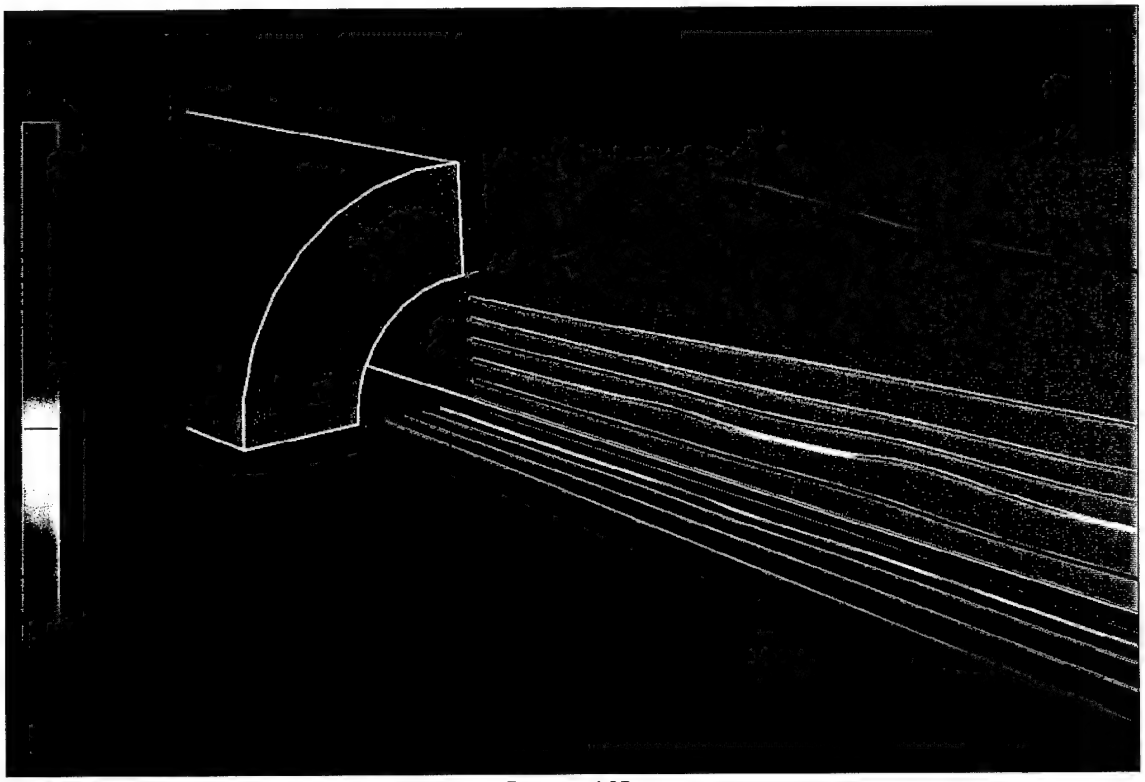

c. $Q_{total}$ = 12Lpm

Figure 16. Particle traces for nozzle with capillary moved in 5.0mm

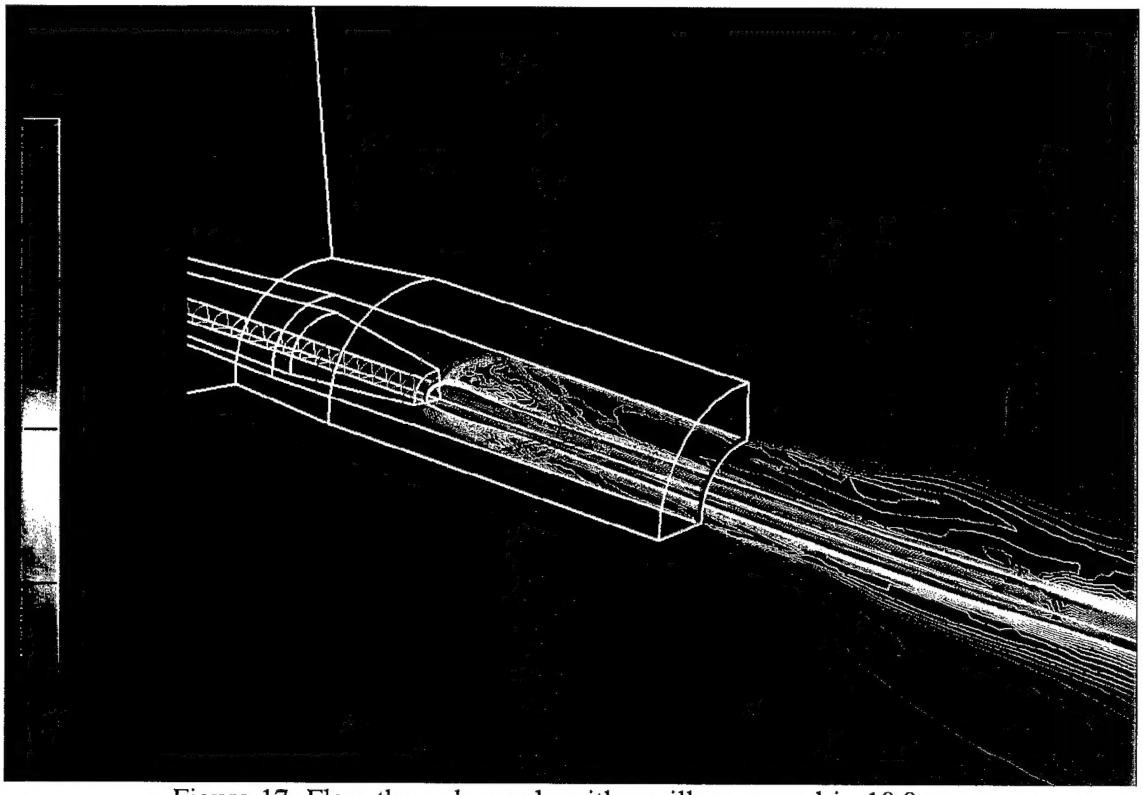

Figure 17. Flow through nozzle with capillary moved in 10.0mm, $Q_{total}$ = 4Lpm, absolute velocity contours

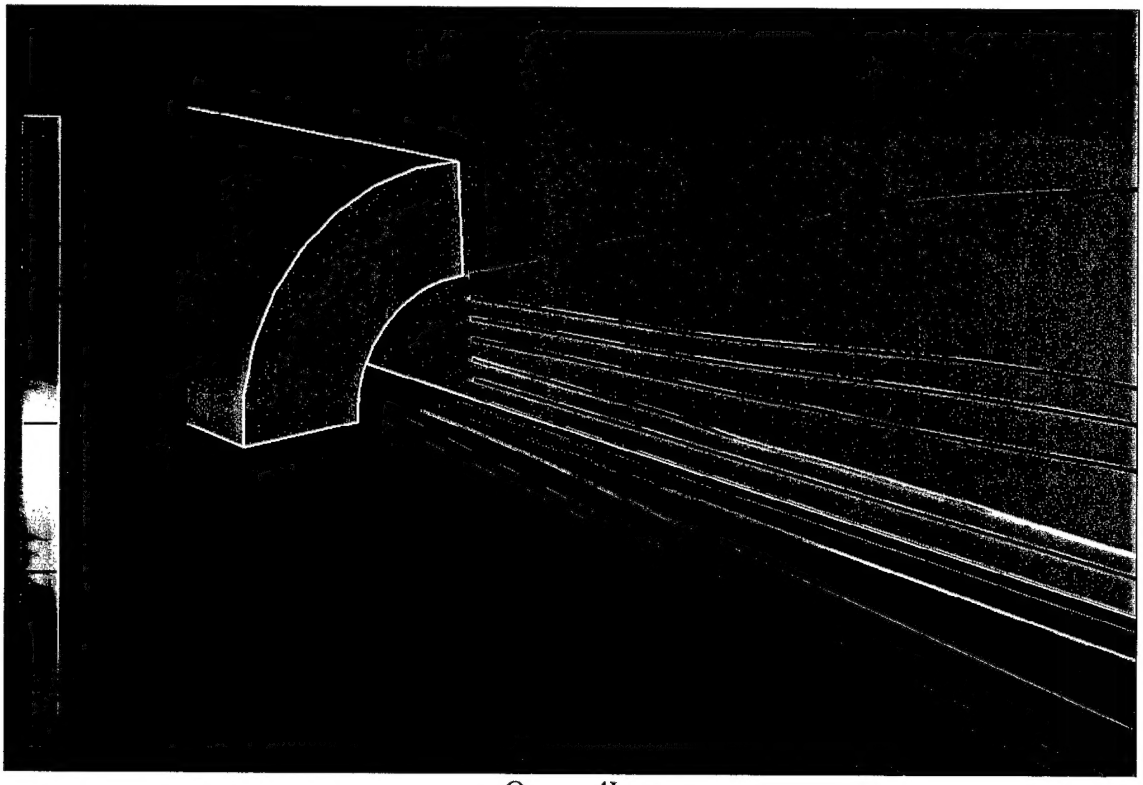

a. $Q_{total}$ = 4Lpm

Figure 18. Particle traces for nozzle with capillary moved in 10.0mm

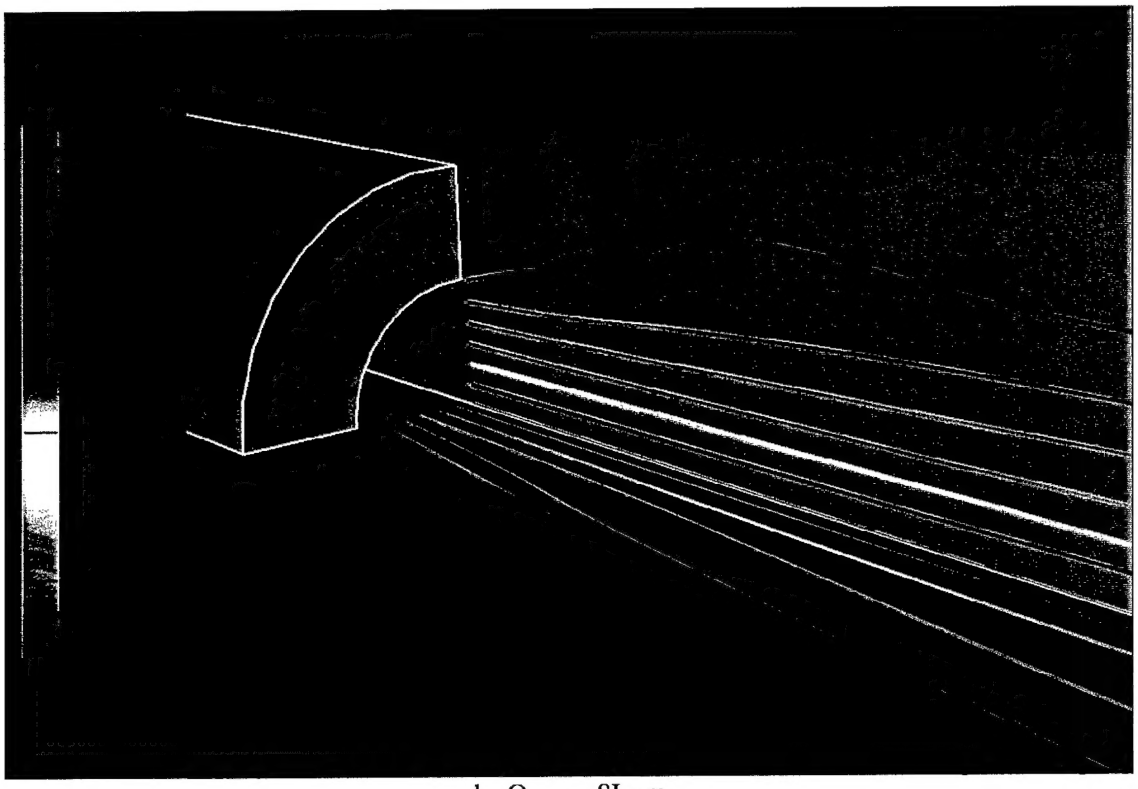

b. $Q_{total}$ = 8Lpm

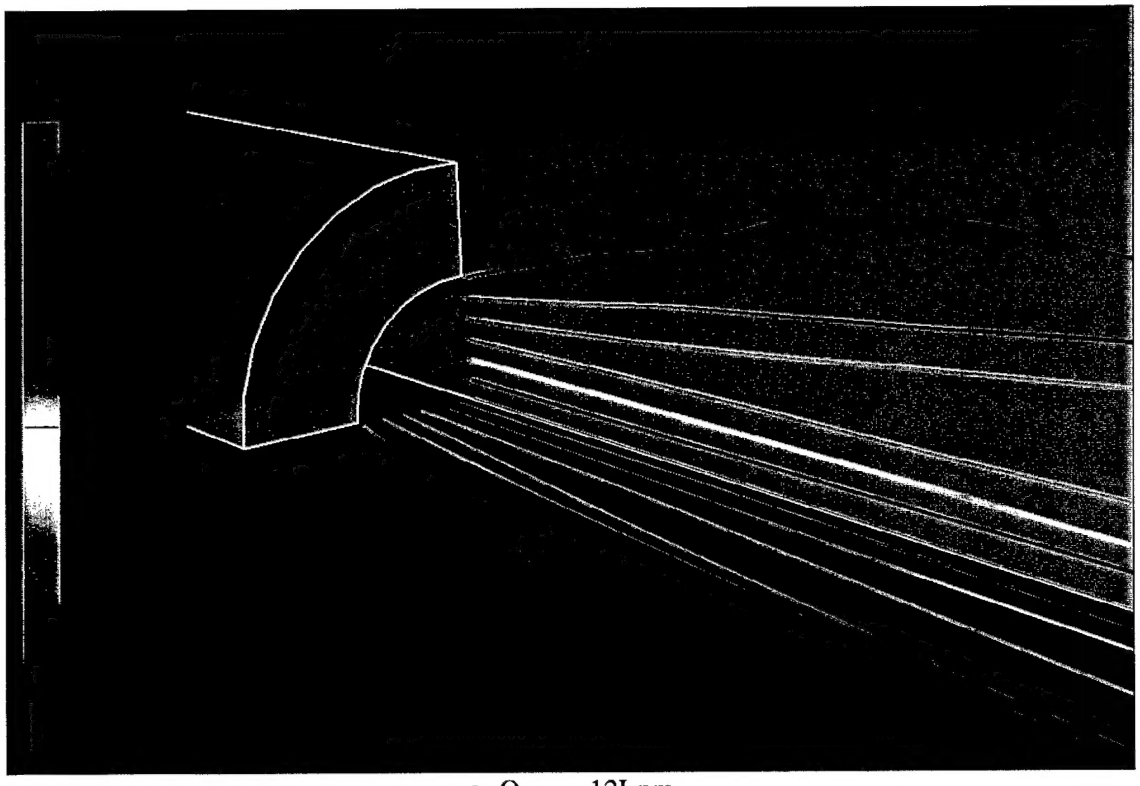

c. $Q_{total}$ = 12Lpm

Figure 18. Particle traces for nozzle with capillary moved in 10.0mm

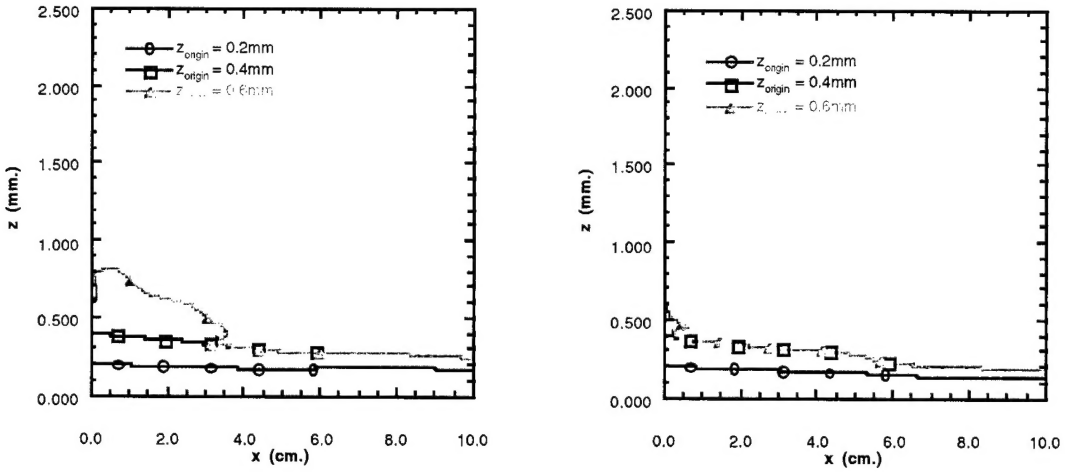


a. $Q_{total}$ = 4Lpm b. $Q_{total}$ = 12Lpm

Figure 19. Particle traces for nozzle with flush capillary

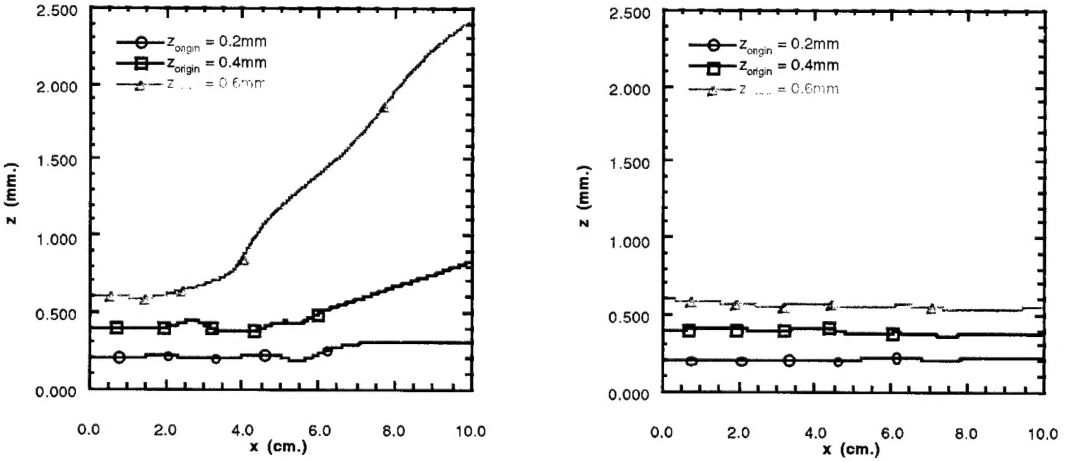


a. $Q_{total}$ = 4Lpm b. $Q_{total}$ = 12Lpm

Figure 20. Particle traces for nozzle with capillary moved in 5.0mm

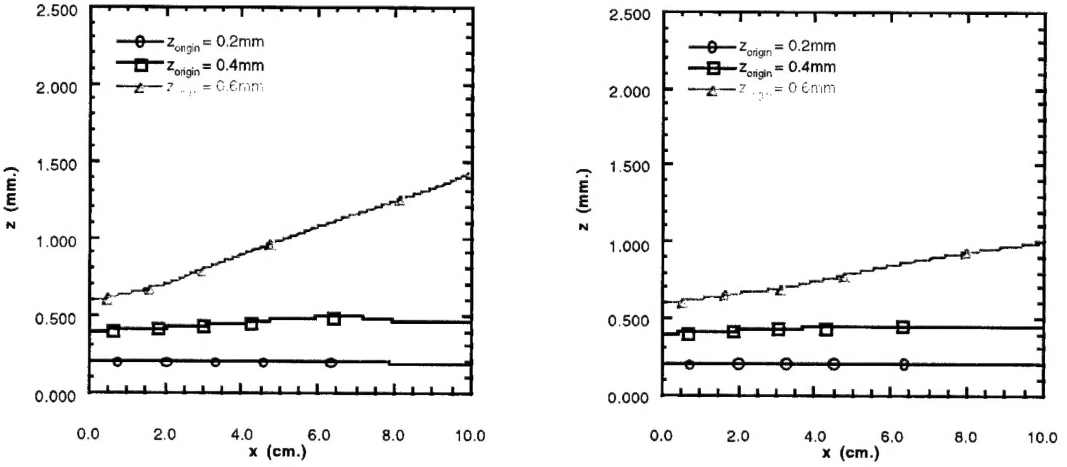


a. $Q_{total}$ = 4Lpm b. $Q_{total}$ = 12Lpm

Figure 21. Particle traces for nozzle with capillary moved in 10.0mm

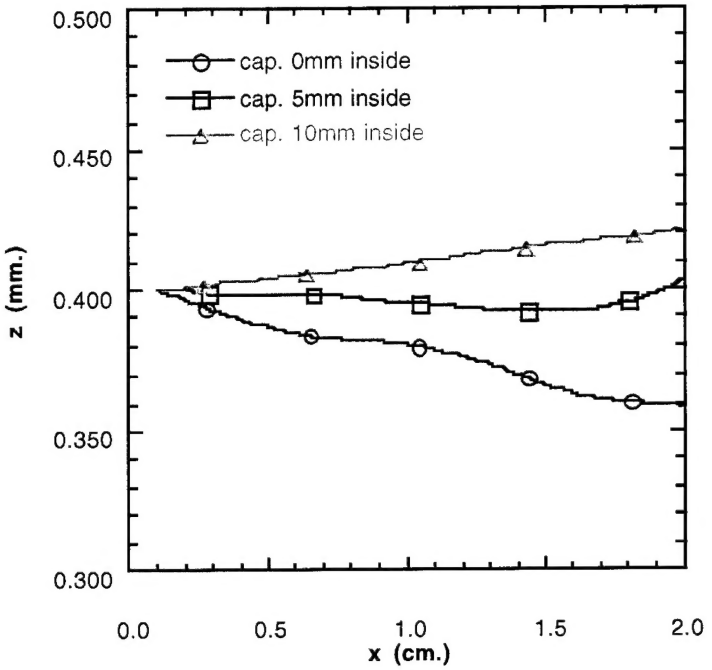


a. $Q_{total}$ = 4Lpm

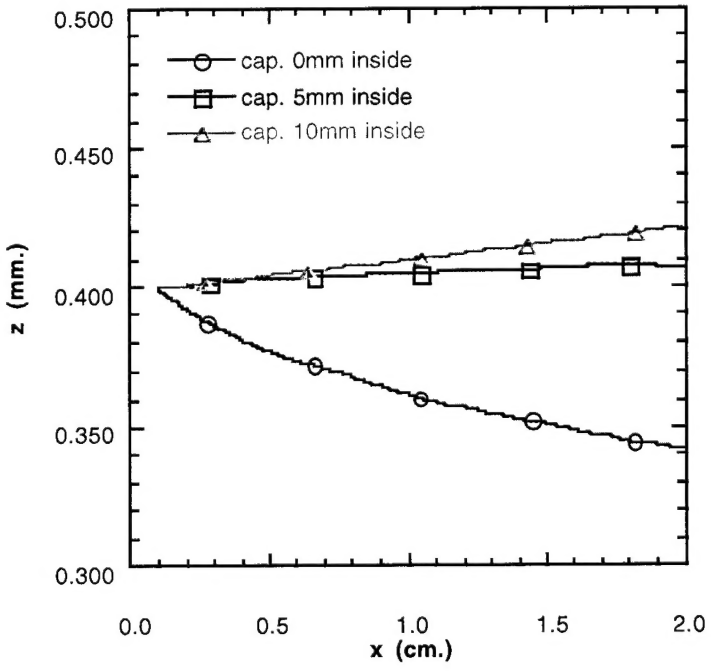


b. $Q_{total}$ = 12Lpm

Figure 22. Effect of capillary position on particle traces